Flux Barrier and Skew Design Optimisation of Reluctance Synchronous Machines

Eduan Howard, *Student Member, IEEE,* , Maarten J. Kamper, *Senior Member, IEEE* and Stiaan Gerber, *Student Member, IEEE,*

***Abstract*—In this paper an investigation into an alternative reluctance synchronous machine rotor flux barrier topology creation technique is presented. The technique investigated implements a high number of flux barrier variables with an alternative asymmetric rotor structure topology in combination with optimisation and finite element analysis. The investigation focuses on maximising average torque and minimising torque ripple in order to study the possibility of achieving acceptable torque ripple machine parameters without implementing rotor skew as torque ripple reduction technique. A further investigation into the effect of rotor skew on the proposed topology is conducted followed by the manufacturing of the proposed flux barrier prototype and testing.**

I. Introduction

With the ever increasing emphasis on efficiency and cost reduction, the interest in reluctance synchronous machines (RSM) has increased during the past decade. This interest is driven by not only the robustness, efficiency and simplicity of the RSM but also by the fact that cost of rare-earth magnets is increasing and the market stability is decreasing of rare-earth magnets in interior permanent magnet machines.

The main focus, depending on application, of most RSM design optimisation is on the maximising of average torque (T_A), within the limits of an allowable volume, and minimising the torque ripple (T_R). The latter is conventionally achieved by rotor skewing and stator cording in order to reduce the air-gap harmonics that produce a high T_R. In this paper, the possibility of both maximising T_A and minimising T_R without implementing rotor skew techniques to achieve acceptable T_R values is investigated. A further investigation into the effect of rotor skew on the topology is also done to even further reduce T_R values.

A large part of the design of a RSM is focused on the rotor creation, and more specifically the type of flux barrier topology and its creation procedure. With the latter in mind, two creation techniques were summarised in [1], the first of which is implemented in this paper. The procedure is based on a predetermined basic barrier structure with a fixed number of variable parameters (barrier tip angle, barrier width, etc). These parameters are numerically optimised with the help of a finite element method (FEM) package that calculates each iteration's relevant machine performance parameters (torque, torque ripple, etc.). Examples of this design procedure can be found in [2]–[6]. The advantage of this approach is that the optimisation inherently takes complex phenomena like torque harmonics and cross saturation into account.

In a further investigation into existing rotor topologies implemented in RSM design, three basic base topology shapes started to emerge with combinations and small variations between specific research projects. These three shapes are illustrated in Fig. 1.

This work is supported by ABB Corporate Research, Sweden.

Eduan Howard, Maarten J. Kamper and Stiaan Gerber is with the Department of Electrical and Electronic Engineering, Stellenbosch University, Stellenbosch, South Africa, phone: +27(0)21-808-4323; fax: +27(0)21-808-3951; e-mail: kamper@sun.ac.za.

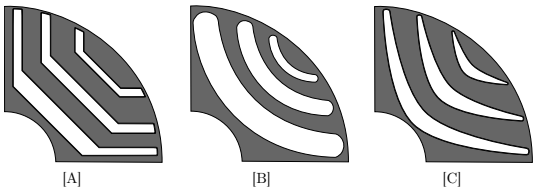

Fig. 1. Rotor flux barrier profiles of four pole RSMs in literature.

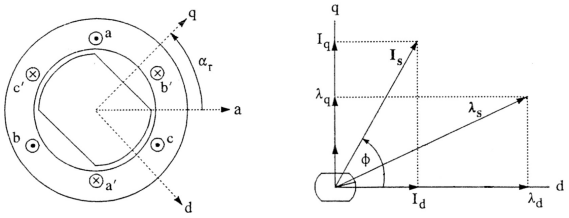

Fig. 2. Cross-section of the RSM and space phasor diagram fixed in the rotor reference frame [2].

The first of these topologies, A in Fig. 1, is created by implementing straight lines to create the flux barriers with examples of the topology researched in [4] and [7]. The second topology, B, was created by implementing circles to create the respective flux barriers with examples of this topology researched in [2], [3], [8], [9].

The initial problem investigated in topologies A and B is the lack of freedom that the optimisation algorithm has as a result of the predetermined barrier shape selected. In an effort to solve this problem, topology C that implements second order polynomials was suggested, with an example of this topology implemented in [10].

In an effort to give the optimiser more freedom in the shaping of the barriers, a combined topology is proposed in this paper which is a combination of both type A and type C procedures. This process is perceived to be a more optimal solution, with examples of similar topologies in [11] and [12], where very low T_R and high efficiencies were obtained. To further increase the freedom of the optimising algorithm, an asymmetric pole structure (ASPS) is proposed with the ASPS line selected on the q-axis in the space phasor diagram in Fig. 2. The selection of this axis for the proposed structure is contrary to the popular trend to implement the d-axis in Fig. 2 as asymmetric line, with examples of this RSM design in [13]–[16] and an illustration of the two asymmetric topologies in Fig. 3. The topology proposed in this paper may have a variation in machine performance depending on the direction of rotation and mode of operation (motor or generator). For this study, a unidirectional machine application is assumed.

The newly suggested rotor topology structure is explained along with a summary of the parameter calculations of the machine and the optimisation techniques implemented in the design. A rotor skew analysis is implemented to further investigate the possibility of T_R reduction.

II. Topology Creation

For the suggested model, two existing stators are implemented to investigate the newly suggested rotor flux barrier

978-1-4799-4775-1/14/$31.00 ©2014 IEEE

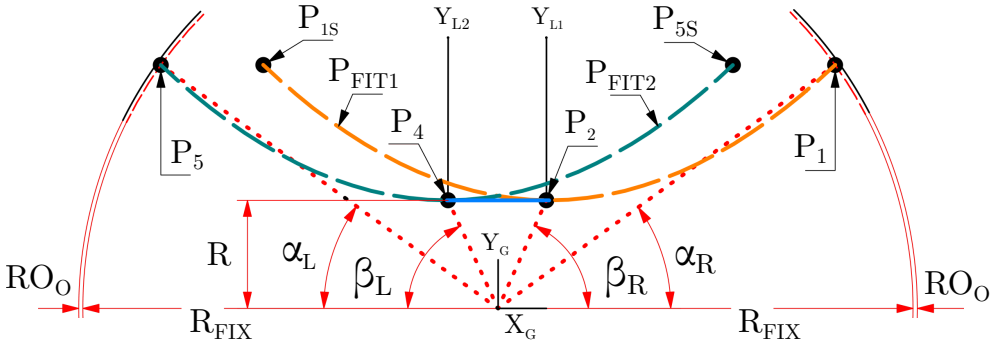

Fig. 4. Flux barrier creation variables with subscript G, the global axis and L, the two local axes.

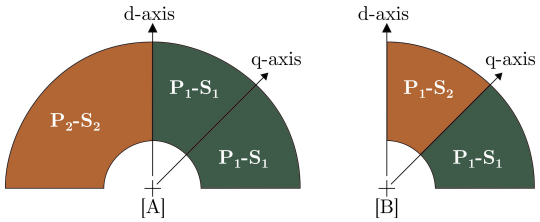

Fig. 3. Four pole asymmetric structure illustrating the different two pole topologies implemented with (A) - Asymmetric rotor structure commonly implemented in RSM rotor design around the d-axis and (B) - Asymmetric rotor structure implemented in this paper around the q-axis

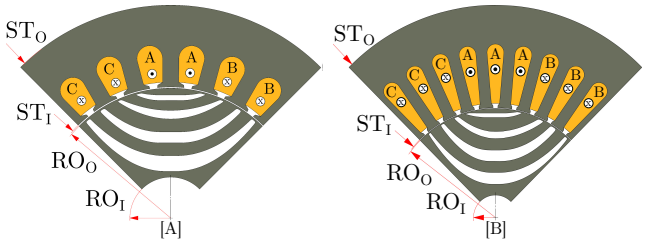

Fig. 5. (A) - 24-Slot RSM with specifications in Table I and RO_O=39.7mm, RO_I=12.5mm, with stack length of 0.122 m and a air gap length of $0.3mm$; (B) - 36-Slot RSM with specifications in Table I and RO_O=52,2m, RO_I=21,5m, with stack length of 0.1334 m and a air gap length of $0.35mm$

TABLE I. STATOR SPECIFICATIONS OF THE 24-SLOT AND 36-SLOT MACHINES (N_{ST}-THE NUMBER OF SERIES TURNS PER PHASE.)

Stator Rated Machine Specifications							
Stator	V $[V]$	I $[A]$	f_e $[Hz]$	ST_I $[m]$	ST_O $[m]$	N_{ST}	J $[A/mm^2]$
24-Slot	400	3.5	50	0.08	0.13	132	±9
36-Slot	150	42	50	0.1051	0.2032	36	±9

topology. The first is an existing 24-slot induction machine stator and the second, an existing 36-slot stator from a RSM machine optimised for topology B by [2] and presented in in Fig. 1. The stators implemented, along with the rotor topologies, are illustrated in Fig. 5. As can be seen in the figure, the central support web commonly implemented ([2], [8], [9], [11], [12]) in the barrier creation for rotor rigidity has been omitted to increase the saliency ratio and hence the performance of the machine as was done by [10].

A. Barrier Construction

An illustration of the new proposed flux barrier topology is shown in Figs. 4 and 6. The main parameters of the topology are points P_1 to P_5 with symmetric points P_{1S} and P_{5S} created around the respective local y-axes Y_{L1} and Y_{L2}. These points are then implemented in two second order polynomial fittings to create the barrier "mid line". The fittings consist of P_{FIT1} through points P_1, P_2 and P_{1S} and P_{FIT2} through points P_{5S}, P_4 and P_5. Finally a horizontal line, connecting the respective polynomial vertex points P_2 and P_4, concludes the barrier "mid line" construction. The width of the barrier is defined by P_{1SP}, P_{3SP} and P_{5SP}, as shown in Fig. 6.

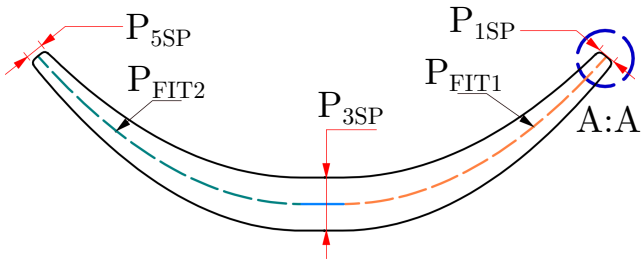

Fig. 6. Flux barrier point width variables.

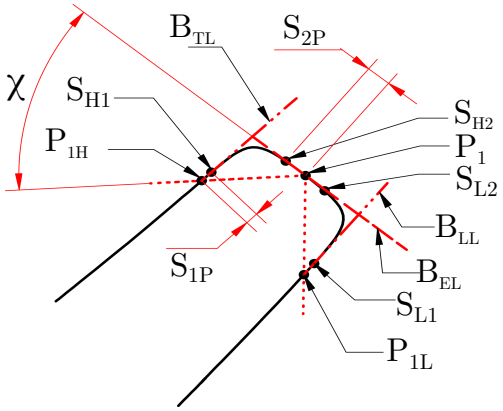

Fig. 7. Bezier Cubic Spline fitting of section **A:A** in Figure 4.

The curve fitting consists of a second order polynomial,

$$p(x) = c_0 + c_1 \cdot x + c_2 \cdot x^2 \tag{1}$$

with the coefficient matrix of the coefficients p in the Vandermonde matrix format with the solution square error of the fitting minimized by

$$E = \sum_{k}^{j=0} |p(x_j) - y_j|^2 \tag{2}$$

Points P_1 and P_5's coordinates consist of a constant pre-set radius R_{FIX} and an angle α as indicated in the figure. The y-axis vertex point coordinates of the two fitted polynomials consist of a vertical displacement R and a lateral displacement angle β specifying the displacement to vertex points P_2 and P_4 respectively. Concluding the barrier construction, thus far five variables, [α_R, β_L, R, P_{3sp} and P_{1sp}], are used to create one barrier for the symmetric case, with the addition of 3 variables [α_L, β_L, and P_{5sp}] for the asymmetric case.

Because of the extreme sensitivity of T_R in RSMs as the low percentage T_R values are approached, as presented in [15], the end tips of the barriers are additionally adjusted with the addition of more variability for the optimisation algorithm to utilise.

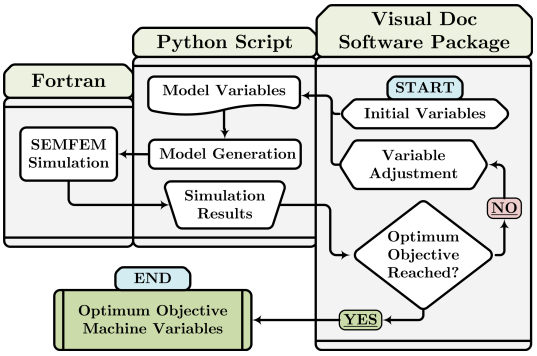

Fig. 8. Optimisation flow diagram implementing a Python script to link the optimisation package VisualDoc with the FE package SEMFEM for topology optimisation.

B. Barrier Tip Construction

Fig. 7 is an illustration of one barrier tip with its location in section **A:A** in Fig. 6. In this figure, the original barrier lines are visible and annotated by the Barrier Top Limit (B_{TL}), the Barrier Lower Limet(B_{LL}) and the Barrier End Limit(B_{EL}).

In order to reduce the sharp force concentrating areas at the tips of the barriers and to give the optimiser more variability in the most sensitive T_R area, a Bezier Cubic Spline fitting is utilised. This spline fitting consists of four points: a start point, P_{1_H} or P_{1_L}, a stopping point P_1 and two points indicating the departure angles from start point to end point, points S_{H1} and S_{H2} or points S_{L1} and S_{L2}. The locations of P_{1_H} and P_{1_L} on the B_{TL} and B_{LL} lines are determined by the angle χ.

With these added variables, each symmetric barrier now consists of eight variables namely [α_R, β_R, R, P_{3sp}, P_{1sp}, χ, S_{1P} and S_{2P}], with each variable consisting of a matrix containing each respective barrier's correlating variable.

Four barriers are chosen for the final design in order to reduce T_R as much as possible, as illustrated by [14], where an increase in barriers indicates a decrease in T_R.

III. Optimization

A. Motor Parameter Calculation

For the motor parameter FE simulation, the rated conditions for the respective stators are used as tabulated in Table I. In an attempt to reduce the design optimisation time, an alternative FE simulation package is used, namely SEMFEM, that was developed in house by Gerber [17]. The advantage of this package is its greatly reduced FE simulation solving time as compared to commercial FE simulation packages as a result of its script based interface.

Each FE simulation is set up with the rotor rotating at an angle equivalent to two slot pitches, with the number of steps for the design optimisations set to 50. The machine performance parameter T_R is calculated by

$$T_R = \frac{MAX(T_n) - MIN(T_n)}{T_A} \qquad (3)$$

with N the number of rotor steps in the FE simulation.

B. Optimisation Procedure

For the optimisation, the VisualDoc [18] software package is used. The flow diagram of the optimisation procedure is illustrated in Fig. 8. The simulation time for the 24-slot machine, that includes the reading in of variables, reconstructing the updated topology, setting up the FE package, solving and post-processing is about 30 seconds. The same procedure for the 36-slot machine is concluded in 95 seconds.

The optimisation of the rotor topology consists of two separate strategies as presented in Fig. 9, with the initial

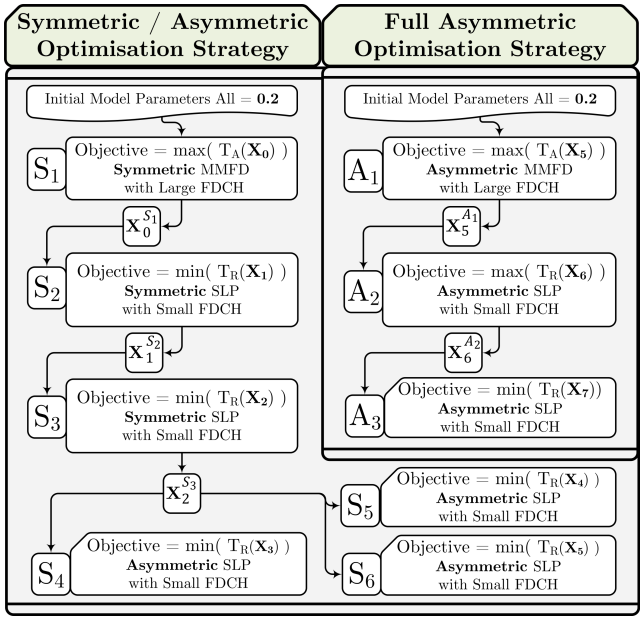

Fig. 9. Optimisation strategies implemented and variable flow diagram, with the superscript 'S' indicating the implementation of the symmetric-asymmetric procedure and superscript 'A' the full-asymmetric optimisation procedure.

TABLE II. Optimisation variables*.

	SAS Optimisation						**FAS** Optimisation		
	X_0	X_1	X_2	X_3	X_4	X_5	X_6	X_7	X_8
α	$\surd_R$	$\surd_R$	$\surd_R$	$\surd_L$	$\surd$	$\surd$	$\surd$	$\surd$	$\surd$
β	$\surd_R$		$\surd_R$		$\surd$	$\surd$	$\surd$		$\surd$
R	$\surd$		$\surd$		$\surd$	$\surd$	$\surd$		$\surd$
P_{1sp}	$\surd$		$\surd$		$\surd$	$\surd$	$\surd$		$\surd$
P_{3sp}	$\surd$		$\surd$		$\surd$	$\surd$	$\surd$		$\surd$
P_{5sp}					$\surd$	$\surd$	$\surd$		$\surd$
χ	$\surd_R$		$\surd_R$		$\surd$	$\surd$	$\surd$		$\surd$
S_1P	$\surd_R$		$\surd_R$		$\surd$	$\surd$			
S_2P	$\surd_R$		$\surd_R$		$\surd$	$\surd$			
θ	$\surd$			$\surd$		$\surd$	$\surd$		

* $\surd_R$ - Right Side, $\surd_L$ - Left Side, $\surd$ - Right & Left Sides
Referring right and left sides of section $P_1 - S_1$ and $P_1 - S_2$ in Fig. 3

strategy a symmetric-asymmetric (SAS) strategy and the second, a full asymmetric strategy (FAS). Both of these strategies optimisation objectives are to maximise T_A and minimise T_R. The initial global search for maximising T_A is conducted by a large relative finite difference step size, followed by an unconstrained minimisation of T_R with small finite difference step size (FDCH).

The objective T_A is maximised by using a gradient based optimisation algorithm namely the Modified Method of Feasible Direction (MMFD); objective T_R is minimized by utilising the optimisation algorithm Sequential Linear Programming (SLP). These specific algorithms were selected after they were found to produce the most accurate results for each respective objective function.

1) Symmetric-Asymmetric Optimisation Strategy: For the initial study on the 24-slot and 36-slot motors, the flux barrier topologies are first symmetrically optimised by maximising $T_A(X_0)$, with the R subscript of variables in X_O at Table II indicating the right side $P_1 - S_1$ section as shown in Fig. 3. This is done in order to speed up the optimisation procedure by reducing the number of variables and in order to provide a base line for comparative optimised asymmetric structures.

For the symmetric optimisation, points P_{5SP}, α_L and β_L are symmetrically generated around the global y-axis from points P_{1SP}, α_R and β_R with the barrier tips symmetrically reproduced for each respective barrier. All variables, includ-

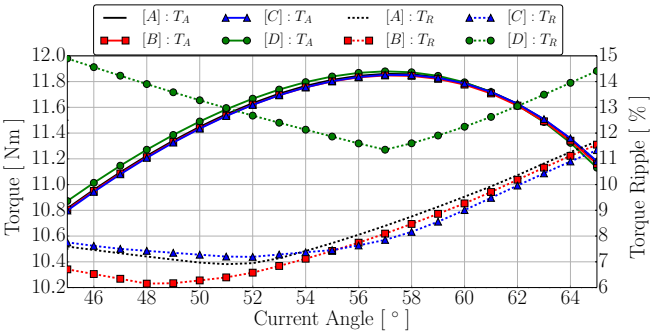

Fig. 10. Symmetric-asymmetric optimisation objective torque ripple and torque results versus current angle of the 24-slot machine with, (A) - $T_R(X_3)$, (B) - $T_R(X_5)$, (C) - $T_R(X_4)$, (D) - $T_R(X_2)$.

ing the rated conditions on the stator are kept constant, excluding the current angle θ which is also allowed to vary between 45 and 90 degrees. The optimisation constraints summarised on the rotor are given by

$$\mathrm{U} = \begin{bmatrix} RO_O \\ RO_I \end{bmatrix} \tag{4}$$

After the symmetric maximisation, the second objective function is symmetrically minimised, using solution variables $X_0^{S_1}$ as start variables. The minimisation is done in two steps by constraining all the variables except those summarised by X_1 in Table II, with objective function $T_R(X_1)$ and secondly with all the variables allowed to vary symmetrically with objective function, $T_R(X_2)$. The latter is conducted with the current angle θ constrained by implementing the variables $X_1^{S_2}$ as start variables. The optimisation result of S_3 in Fig.8 is now implemented in three separate optimisation (S_4, S_5 and S_6 in Fig.8) studies implementing the 24-slot machine in order to determine the effects of the proposed asymmetric topology on the symmetric machine performance results.

The topology optimisation study (S_4) consist of the minimisation of objective function $T_R(X_3)$ with variables X_3 in Table II and with only the current angle and the left symmetric side $P_1 - S_2$ variables allowed to vary. The second and third optimisations (S_5 and S_6) consisted of objective functions $T_R(X_4)$ and $T_R(X_5)$. The variables of X_4 equal those of X_5 with the addition of the current angle θ that is also allowed to vary in X_5.

The performance results of the four optimisation objectives are illustrated in Fig. 10, where the four different topologies found are mapped against the current angle change for the 24-slot machine. The tabulated values for each of the four objectives can be found in Table III. Here, the symmetric maximum T_A and minimum T_R current angle positions of objective S_3, for the 24-slot machine, is taken as the unity values for the per unit value calculations. From this table, the lowest achievable T_R are from S_6, with a 6% reduction in maximum T_A and a 46% reduction in T_R from the symmetric optimisation. From this initial optimisation study, the observation is made that a reduction in T_R is possible with the proposed flux barrier topology without affecting the T_A current angle mapping when implementing the proposed asymmetric flux barrier optimisation. A further observation is made that the maximum T_A point and minimum T_R point are not at the same current angle when implementing the specific asymmetric optimisation strategy.

2) Full Asymmetric Optimisation Strategy: In an attempt to combine the reduction of T_R from $T_R(X_5)$ with the coherent current angle point for high T_A and low T_R from $T_R(X_2)$, a full-asymmetric strategy is implemented. The strategy includes a $T_A(X_6)$ objective function with

TABLE III. SYMMETRIC-ASYMMETRIC OPTIMISATION STRATEGY RESULTS OF THE 24-SLOT MACHINES.

Symmetric-Asymmetric Optimisation Strategy Results						
Stator		θ	T_A		T_R	
Slots	**Objective Function**	[°]	[Nm]	[P.u]	[%]	[P.u]
24	$T_R(X_2)$ - (Max T_A)	57	**11.88**	1.00	11.35	1.00
24	$T_R(X_2)$ - (Min T_R)	57	11.88	1.00	**11.35**	1.00
24	$T_R(X_3)$ - (Max T_A)	57	**11.84**	1.00	7.85	0.69
24	$T_R(X_3)$ - (Min T_R)	52	11.62	0.97	**7.19**	0.33
24	$T_R(X_4)$ - (Max T_A)	57	**11.86**	1.00	8.40	0.74
24	$T_R(X_4)$ - (Min T_R)	51	11.54	0.98	**6.91**	0.61
24	$T_R(X_5)$ - (Max T_A)	57	**11.85**	1.00	8.10	0.71
24	$T_R(X_5)$ - (Min T_R)	48	11.21	0.94	**6.15**	0.54

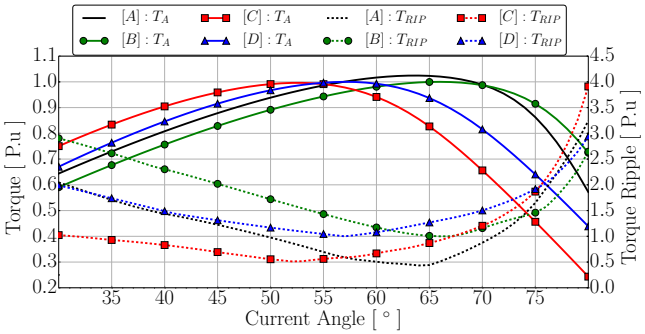

Fig. 11. Full-asymmetric optimisation objective torque ripple and torque results versus current angle comparison for the 24-slot and 36-slot machines with: (A) - $T_R(X_8)$ 36-slot Machine, (B) - $T_R(X_2)$ 36-slot machine, (C) - $T_R(X_8)$ 24-slot machine, (D) - $T_R(X_2)$ 24-slot machine.

variables X_6 as in Tabel II and with the model asymmetrically maximised from the start utilising the MMFD algorithm.

In the initial optimisation study, it is noted that the optimiser maximised variables S_{1P} and S_{2P} to their maximum allowable area. Thus, in the second optimisation, these variables where omitted from the optimisation variables, with an maximum value.

Once again, the two step T_R minimisation discussed in the initial optimisation strategy is repeated, with variables X_7 in Tabel II allowed to vary asymmetrically for $T_R(X_7)$ minimisation, implementing variables $X_6^{A_1}$ as start variables. This optimisation is followed by $T_R(X_8)$ objective minimisation, implementing the result variables $X_7^{A_2}$ from $T_R(X_7)$ as initial values. The latter is conducted with θ constrained at the objective function $T_A(X_6)$ convergence point in order to force the optimiser to seek a mutual coherent maximum T_A, and minimum T_R current angle point as found with the symmetric optimisation model $T_R(X_2)$.

The results of this progress strategy applied to both the 24-slot and 36-slot machines are tabulated in Table IV and illustrated in Fig. 11. In the table the initial full symmetric optimisation $T_R(X_2)$ results of both stators are taken as unity for the per unit calculations. Also shown in the table are the initial $T_A(X_6)$ maximisation results, illustrating a slight drop in T_A during the two step minimization of T_R.

From the figure and table it is clear that achieving a coherent maximum T_A and minimum T_R point is possible with respect to current angle. Furthermore, a minimum torque ripple of 3.9% and 5.7% are achieved for the 36-slot and 24-slot machines respectively. Additionally, a 2% increase in T_A is achieved for the 36-slot machine. The optimised rotor flux barrier topologies laminations of objective $T_R(X_5)$ and objective function $T_R(X_8)$ applied to the two 24-slot and 36-slot machines are illustrated in Fig. 12.

TABLE IV. FULL ASYMMETRIC OPTIMISATION STRATEGY VERSUS FULL-SYMMETRIC OPTIMISATION STRATEGY RESULTS OF THE 24-SLOT AND 36-SLOT MACHINES.

Stator Slots	Objective Function	θ [°]	T_A [Nm]	T_A [P.u]	T_R [%]	T_R [P.u]
Full Symmetric Optimisation Strategy Results						
	$T_R(X_2)$					
24	$\boldsymbol{T_R(X_2)}$ - (Max $\boldsymbol{T_A}$)	57	**11.88**	1.00	11.35	1.00
24	$\boldsymbol{T_R(X_2)}$ - (Min $\boldsymbol{T_R}$)	57	11.88	1.00	**11.35**	1.00
36	$\boldsymbol{T_R(X_2)}$ - (Max $\boldsymbol{T_A}$)	66	**75.23**	1.00	8.49	1.00
36	$\boldsymbol{T_R(X_2)}$ - (Min $\boldsymbol{T_R}$)	66	75.23	1.00	**8.49**	1.00
Full Asymmetric Optimisation Strategy Results						
	$T_R(X_8)$					
24	$\boldsymbol{T_R(X_6)}$ - (Max $\boldsymbol{T_A}$)	52.2	**11.93**	1.00	51.54	4.54
24	$\boldsymbol{T_R(X_6)}$ - (Min $\boldsymbol{T_R}$)	52.2	11.93	1.00	**51.54**	4.54
24	$\boldsymbol{T_R(X_8)}$ - (Max $\boldsymbol{T_A}$)	52.5	**11.83**	1.00	5.72	0.67
24	$\boldsymbol{T_R(X_8)}$ - (Min $\boldsymbol{T_R}$)	52.5	11.83	1.00	**5.72**	0.67
36	$\boldsymbol{T_R(X_6)}$ - (Max $\boldsymbol{T_A}$)	64	**78.53**	1.04	52.79	6.22
36	$\boldsymbol{T_R(X_6)}$ - (Min $\boldsymbol{T_R}$)	64	78.53	1.04	**52.79**	6.22
36	$\boldsymbol{T_R(X_8)}$ - (Max $\boldsymbol{T_A}$)	64	**77.06**	1.02	3.90	0.46
36	$\boldsymbol{T_R(X_8)}$ - (Min $\boldsymbol{T_R}$)	64	77.06	1.02	**3.90**	0.46

[A] [B] [C]

Fig. 12. Laminations of optimisation objective results by objective functions: (A) - $T_R(X_5)$ Lamination 24-slot Machine, (B) - $T_R(X_8)$ Lamination 24-slot Machine, (C) - $T_R(X_8)$ Lamination 36-slot Machine

IV. EFFECT OF ROTOR SKEW ON PROPOSED TOPOLOGY.

In this section, the effect of rotor skew on the five optimum topologies optimised is investigated. These topologies are: $T_R(X_2)$, for the 24-slot and 36-slot machines, $T_R(X_5)$ of the 24-slot machine together with both the $T_R(X_8)$ objectives from the 24-slot and 36-slot machines. The process of investigation included a T_R contour mapping versus current and skew angle. The average torque for each step of the mapping is calculated by dividing the machine into 5 respective machines as described by [8]. Equation (5) is then used to calculate T_A and (3) to calculate T_R from the results of (5).

$$T_A = \frac{1}{k}\sum_{i=1}^{k} T_i \qquad [k=5] \tag{5}$$

The results of the T_R contour mapping for the initial symmetric-asymmetric optimisation strategy for the two implemented stator machines are illustrated in Figs. 13, 14 and 16. The full asymmetric optimisation strategy T_R contour mapping results for the two machines in the second optimisation strategy are illustrated in Fig. 15 and 17. From these figures, the traditional one slot pitch skew for minimum torque ripple is clearly evident at the 15° area for the 24-slot machine and at the 10° area in the 36-slot machine. Additionally, in the 24-slot machine mappings, a second low T_R area in the 7° to 11° skew range is identified in all three 24-slot machine mapping figures, with an additional low torque ripple area in the 4° to 10° skew range for the 36-slot machine mappings.

For the investigation of the 36-slot mapping, two additional angles, 3.0° or 4.0° and 8.0°, are selected for investigation along with the one slot pitch angle and unskewed machine. For the 24-slot machine, one additional angle per topology is selected which includes a 10.6° skew

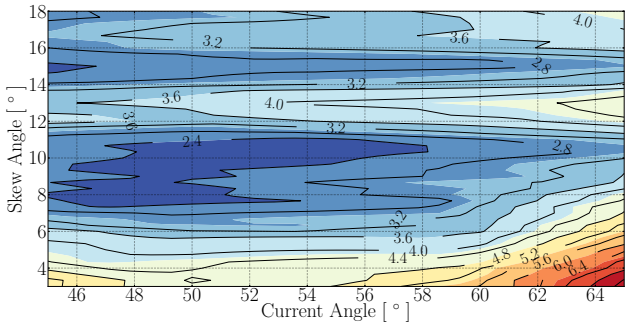

Fig. 13. Torque ripple versus skew and current angle mapping of the full-symmetric optimisation objective function $T_R(X_2)$ of the 24-slot machine with the one slot pitch at 15.0°.

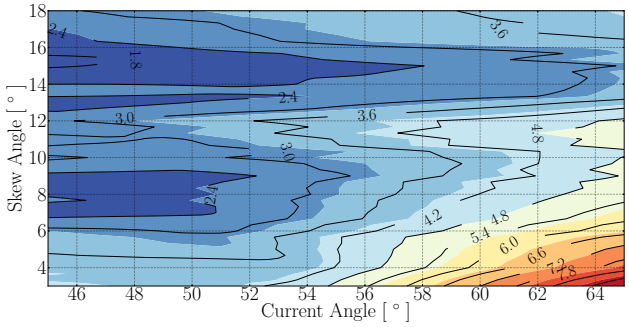

Fig. 14. Torque ripple versus skew and current angle mapping of the symmetric-asymmetric optimisation objective function $T_R(X_5)$ of the 24-slot machine with the one slot pitch at 15.0°.

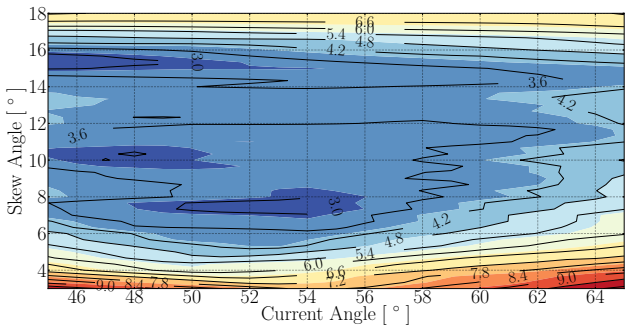

Fig. 15. Torque ripple versus skew and current angle mapping of the full-asymmetric optimisation objective function $T_R(X_8)$ of the 24-slot machine with the one slot pitch at 15.0°.

angle for Fig. 13's mapping, a 9.2° skew angle for Fig. 14's mapping and a 7.6° skew angle for Fig. 15's mapping. The results of this investigation are tabulated in Table V with the 0.0° skew results taken as the unity value for the per unit calculation values for each machine analysed. Comparative current angle maps for the investigated machines form the symmetric-asymmetric optimisation strategy objective $T_R(X_5)$ and full-asymmetric optimisation objective $T_R(X_8)$ for the 36-slot and 24-slot machines with selected skew angles are illustrated in Figs. 18 and 19.

From Table V's results it is evident that although the lowest possible T_R is achieved with the traditional one slot pitch skew in most cases, this angle is not the optimum if T_A is also taken into account. The variation of T_R and T_A with skew angle and current angle is clearly visible in Fig. 18 and 19.

Considering the two T_R mappings of the 24-slot machine for the two different topologies found by $T_R(X_5)$ and $T_R(X_8)$ in Fig.s 14 and 15, it is clear that the effective angle for rotor skew heavily depends on the specific rotor topology. Furthermore, an interesting trend is observed with the 24-slot machine, where the three mappings have low T_R values in the 60% to 70% slot pitch angle areas. These

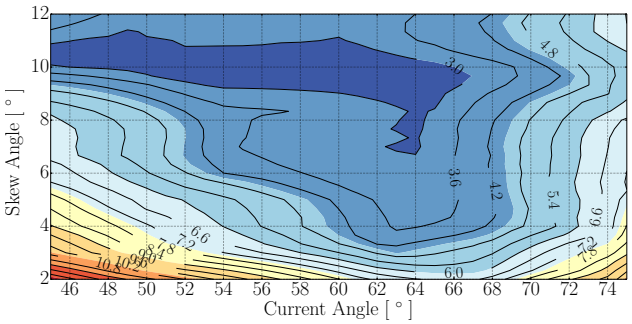

Fig. 16. Torque ripple versus skew and current angle mapping of the full-symmetric optimisation objective function $T_R(X_2)$ of the 36-slot machine with the one slot pitch at 10.0°.

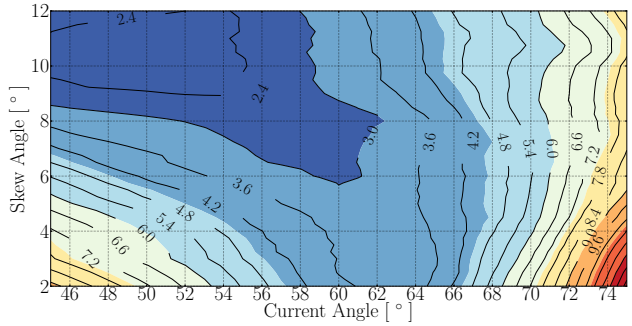

Fig. 17. Torque ripple versus skew and current angle mapping of the full-asymmetric optimisation objective function $T_R(X_8)$ of the 36-slot machine with the one slot pitch at 10.0°.

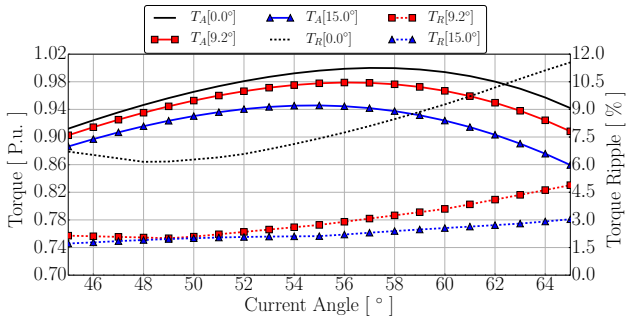

Fig. 18. Symmetric-asymmetric optimisation objective function $T_R(X_5)$ average torque, torque ripple versus current angle for the selected skew angles 0.0°, 9.2° and 15.0° for the 24-slot machine.

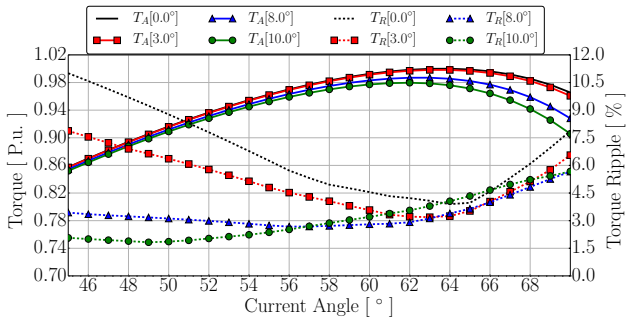

Fig. 19. Full-asymmetric optimisation objective function $T_R(X_8)$ average torque, torque ripple versus current angle for the selected skew angles 0.0°, 3.0°, 8.0° and 10.0° for the 36-slot machine.

angles provide improved machine performance parameters compared to the conventional one slot pitch skew.

In order to verify the optimised topologies, objective function $T_R(X_5)$ is selected for manufacturing, which includes the 9.2° skew angle as perceived to be the optimum skew angle for the objectives topology as in Table V. The machine is tested by incorporating the manufactured RSM connected to a induction machine with torque sensor

TABLE V. SKEW ANGLE RESULTS OF THE SYMMETRIC-ASYMMETRIC AND FULL-ASYMMETRIC OPTIMISATION STRATEGY TOPOLOGIES.

Skew Angle Mapping						
Stator Slots	**Skew Angle**	θ [°]	T_A [Nm]	T_A [P.u]	T_R [%]	T_R [P.u]
Symmetric-Asymmetric Strategy						
	$F1_2(X_2)$					
24	**0.0°** - (Max T_A)	57	**11.88**	1.00	11.35	1.00
24	**0.0°** - (Min T_R)	57	11.88	1.00	**11.35**	1.00
24	**10.6°** - (Max T_A)	53	**11.50**	0.97	2.14	0.19
24	**10.6°** - (Min T_R)	53	11.47	0.97	**2.1**	0.19
24	**15.0°** - (Max T_A)	50	**11.19**	0.94	2.6	0.23
24	**15.0°** - (Min T_R)	45	11.0	0.93	**2.28**	0.20
36	**0.0°** - (Max T_A)	66	**75.23**	1.00	8.97	1.00
36	**0.0°** - (Min T_R)	66	75.23	1.00	**8.97**	1.00
36	**4.0°** - (Max T_A)	66	**74.98**	1.00	3.83	0.43
36	**4.0°** - (Min T_R)	66	74.66	1.00	**2.87**	0.32
36	**8.0°** - (Max T_A)	65	**74.22**	0.99	3.15	0.35
36	**8.0°** - (Min T_R)	53	74.19	0.99	**2.87**	0.32
36	**10.0°** - (Max T_A)	64	**73.66**	0.98	2.66	0.30
36	**10.0°** - (Min T_R)	63	73.58	0.98	**2.53**	0.28
	$F1_2(X_5)$					
24	**0.0°** - (Max T_A)	57	**11.85**	1.00	8.10	1.32
24	**0.0°** - (Min T_R)	48	11.21	0.95	**6.15**	1.00
24	**9.2°** - (Max T_A)	56	**11.59**	0.98	2.90	0.47
24	**9.2°** - (Min T_R)	49	11.18	0.94	**2.01**	0.33
24	**15.0°** - (Max T_A)	55	**11.20**	0.95	2.12	0.35
24	**15.0°** - (Min T_R)	45	10.50	0.89	**1.72**	0.28
Full Asymmetric Strategy						
	$F2_2(X_8)$					
24	**0.0°** - (Max T_A)	53	**11.83**	1.00	5.72	1.00
24	**0.0°** - (Min T_R)	53	11.83	1.00	**5.72**	1.00
24	**7.6°** - (Max T_A)	56	**11.66**	0.99	3.28	0.57
24	**7.6°** - (Min T_R)	54	11.62	0.99	**2.84**	0.50
24	**15.0°** - (Max T_A)	49	**11.18**	0.95	2.58	0.45
24	**15.0°** - (Min T_R)	45	10.99	0.93	**2.27**	0.40
	$F2_2(X_8)$					
36	**0.0°** - (Max T_A)	64	**77.06**	1.00	3.90	1.00
36	**0.0°** - (Min T_R)	64	77.06	1.00	**3.90**	1.00
36	**3.0°** - (Max T_A)	63	**76.92**	1.00	3.19	0.82
36	**3.0°** - (Min T_R)	63	76.92	1.00	**3.19**	0.82
36	**8.0°** - (Max T_A)	63	**76.05**	0.98	3.12	0.80
36	**8.0°** - (Min T_R)	56	74.23	0.96	**2.68**	0.69
36	**10.0°** - (Max T_A)	62	**75.49**	0.97	3.56	0.91
36	**10.0°** - (Min T_R)	49	69.24	0.90	**1.83**	0.47

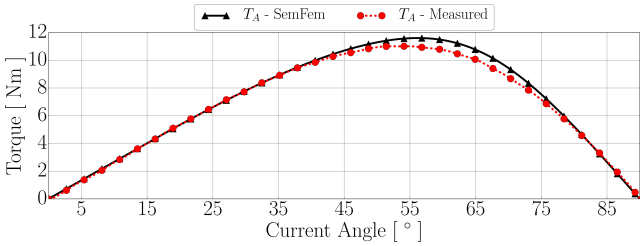

Fig. 20. Measured T_A results plotted again FE simulation of the manufactured 9.2°, objective function $T_R(X_5)$ machine.

separating them.

The measured results of the manufactured rotor are illustrated in Fig. 20 and 21, with the measured T_A values closely correlating simulated values across the current angle range. A variation at rated conditions is however observed, with the measured rated T_A equal to 11.0 Nm, compared to the 11.6 Nm simulated. Figure 21 illustrates a harmonic comparison between the measured and simulated torque ripple harmonics with a slight increase in measured harmonics.

The variation between T_A and T_R for the measured and simulated values is as a possible result of the inaccurate

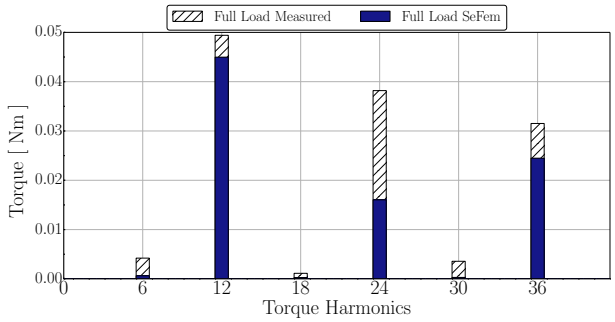

Fig. 21. Torque ripple harmonic plot of the measured torque, with rated conditions at 20 r/min. "Noise" harmonics from test bench were filtered out in order to more clearly illustrate the fundamental simulated and measured harmonics.

reproduction of the stator in the FE package and/or the unknown material properties of the stator.

V. Conclusion

In this paper an alternative asymmetric flux barrier technique is proposed in combination with design optimisation to maximise average torque and minimise torque ripple. It is shown that by implementing a relatively high number of variables of between 29 to 37 a torque ripple of 5.7% and 3.9% is achievable for the 24-slot and 36-slot machines stators respectively without implementing rotor skew. Moreover, it is shown that there is no drop in T_A when comparing the full-symmetric with the full-asymmetric optimisations, with an average torque ripple reduction of 30 to 50% for the 24-slot and 36-slot machines respectively. It is further shown that a torque ripple of below 3.0% is achievable by implementing rotor skew for both 24-slot and 36-slot machines. The latter is achieved with rotor skew angles of between 60 to 70% of a slot pitch angle for the 24-slot machine and between 30 to 80% for a 36-slot machine. The rotor skew analysis illustrates that rotor skew angle not only heavily depends on the specific stator topology but also on the rotor topology. The average torque comparison between simulated and measured results agree well with the torque ripple harmonic comparison between the measured and simulated values also correlating well, with a slight increase in measurement harmonics.

References

[1] A. Vagati, A. Canova, M. Chiampi, M. Pastorelli, M. Repetto, I. Elettrica, and I. Politecnico, "Improvement of Synchronous Reluctance Motor Design through Finite-Element Analysis," *Industry Applications Conference, 1999. Thirty-Fourth IAS Annual Meeting. Conference Record of the 1999 (IEEE)*, pp. 862–871, 1999.

[2] M. Kamper, F. Van der Merwe, and S. Williamson, "Direct finite element design optimisation of the cageless reluctance synchronous machine," *IEEE Transactions on Energy Conversion*, vol. 11, no. 3, pp. 547–555, 1996.

[3] G. Pellegrino, P. Bari, and V. Orabona, "FEA-based multi-objective optimization of IPM motor design including rotor losses," *Electric Machines & Drives Conference (IEMDC), 2013 IEEE International*, pp. 3659–3666, 2010.

[4] R.-R. Moghaddam, F. Magnussen, and C. Sadarangani, "Novel rotor design optimization of Synchronous Reluctance Machine for low torque ripple," *2012 XXth International Conference on Electrical Machines*, pp. 720–724, Sept. 2012.

[5] G. Pellegrino, S. Member, F. Cupertino, and C. Gerada, "Barriers shapes and minimum set of rotor parameters in the automated design of Synchronous Reluctance machines," *Electric Machines & Drives Conference (IEMDC), 2013 IEEE International*, pp. 1204–1210.

[6] F. Cupertino, B. Dei, and C. Gerada, "Design of synchronous reluctance machines with multi-objective optimization algorithms," *Electric Machines & Drives Conference (IEMDC), 2013 IEEE International*, pp. 1858–1865, 2013.

[7] M. J. Kamper and W. T. Villet, "Design and performance of compensated reluctance synchronous machine drive with extended constant power speed range," *2012 IEEE Energy Conversion Congress and Exposition (ECCE)*, pp. 4330–4337, Sept. 2012.

[8] X. Bomela and M. Kamper, "Effect of stator chording and rotor skewing on average torque and torque ripple of reluctance synchronous machine," *1999 IEEE Africon. 5th Africon Conference in Africa (Cat. No.99CH36342)*, vol. 2, pp. 687–690, 1999.

[9] M. H. a. Prins, C. W. Vorster, and M. J. Kamper, "Reluctance synchronous and field intensified-PM motors for variable-gear electric vehicle drives," *2013 IEEE Energy Conversion Congress and Exposition*, pp. 657–664, Sept. 2013.

[10] M. H. A. C. W. Villet, W T. Prins and M. J. Kamper, "Saliency performance investigation of Synchronous Machines for Position Sensorless Controlled EV drives," *In Sensorless Control for Electrical Drives (SLED)*, 2013.

[11] a. Fratta, G. Troglia, a. Vagati, and F. Villata, "Evaluation of torque ripple in high performance synchronous reluctance machines," *Conference Record of the 1993 IEEE Industry Applications Conference Twenty-Eighth IAS Annual Meeting*, pp. 163–170, 1993.

[12] A. Vagati, M. Pastorelli, G. Franceschini, and C. Petrache, "Design of Low-Torque-Ripple Synchronous Reluctance Motors," *IEEE Transactions on Industry Applications*, vol. 34, no. 4, pp. 758–765, 1998.

[13] P. Alotto, M. Barcaro, N. Bianchi, and M. Guarnieri, "Optimization of IPM Motors with Machaon Rotor Flux Barriers," *Electromagnetic Field Computation (CEFC), 2010 14th Biennial IEEE Conference on*, vol. 45, p. 35131, 2010.

[14] M. Ferrari, N. Bianchi, A. Doria, and E. Fornasiero, "Design of synchronous reluctance motor for hybrid electric vehicles," *2013 International Electric Machines & Drives Conference*, pp. 1058–1065, May 2013.

[15] N. Bianchi, M. Degano, and E. Fornasiero, "Sensitivity Analysis of Torque Ripple Reduction of Synchronous Reluctance and Interior PM Motors," *2012 IEEE Energy Conversion Congress and Exposition (ECCE)*, pp. 1842–1849, 2013.

[16] M. Ferrari, N. Bianchi, and E. Fornasiero, "Rotor saturation impact in synchronous reluctance and PM assisted reluctance motors," *2013 IEEE Energy Conversion Congress and Exposition*, pp. 1235–1242, Sept. 2013.

[17] S. Gerber, "A finite element based optimisation tool for electrical machines." Thesis (MSc (Electrical and Electronic Engineering))–University of Stellenbosch, 2011. [Available Online - http://hdl.handle.net/10019.1/6635].

[18] Vanderplaats Research & Development Inc., Colorado Springs, *VisualDOC User Manual*, version 6.0 ed.

VI. Biographies

Eduan Howard (S'14) He received the B.Eng. degree in mechanical engineering from the University of Stellenbosch, Matieland, South Africa in 2012. He is currently working towards the completion of the M.Sc. (Eng.) degree at the Department of Electrical and Electronic Engineering at the University of Stellenbosch. His current research focus is on reluctance synchronous machines for wind turbine purposes and includes the optimising of reluctance synchronous machine technologies, including computer-aided design.

Maarten J. Kamper (SM'2008) received the M.Sc. (Eng.) degree in 1987 and the Ph.D. (Eng.) degree in 1996 both from the University of Stellenbosch, Stellenbosch, South Africa. He has been with the academic staff of the Department of Electrical and Electronic Engineering, University of Stellenbosch, since 1989, where he is currently a Professor of electrical machines and drives. His research interests include computer-aided design and control of reluctance, permanent magnet and induction machine drives. Prof. Kamper is a South African National Research Foundation Supported Scientist and a Registered Professional Engineer in South Africa.

Stiaan Gerber (S'13) He received his BEng (cum laude) in the field of Electrical and Electronic Engineering with Computer Science at Stellenbosch University in 2008 and his MScEng (cum laude) in 2011. He is currently studying towards his PhD in the field of electrical machines, with specific focus on magnetically geared electrical machines. His main interests in the engineering field are electrical machine design, numerical optimization, renewable energy power generation and finite element methods.